Daily reservoir-scale subsurface monitoring using ambient seismic noise

Sjoerd de Ridder and Biondo Biondi

ABSTRACT

Seismic interferometry is applied to continuous seismic recordings spanning five days and over 2200 stations at the Valhall Life-of-Field Seismic (LOFS) array in the Norwegian North Sea. We retrieve both fundamental-mode and first-overtone Scholte-waves by cross-correlation. Ambient-seismic-noise tomography (ASNT) using the vertical component of this dense array produces group-velocity maps of fundamental-mode Scholte waves with high repeatability from only 24 hours of recording. This repeatability makes daily reservoir-scale near-surface continuous monitoring of the subsurface feasible. Such monitoring may detect production-related changes over a long time-scale (months to years) and may be useful for early detection of short time-scale hazards (days to weeks) such as migrating gases and fluids. We validate our velocity maps by comparing them with maps obtained independently from controlled-source data.

INTRODUCTION

Reservoir monitoring using controlled-source seismic surveying is a well-established technique. One survey provides an image of the subsurface at one given time. Repeated seismic surveys provide differential seismic images that show how the subsurface changed over time. A permanent ocean-bottom-cable (OCB), called the Life-of-Field Seismic (LOFS) array (Kommedal et al., 2004), was installed just under the seabed at the Valhall Field in the Norwegian North in 2003. Conventional controlled-source seismic surveying provides subsurface images after expensive seismic acquisition, processing, and imaging procedures, and only at a few snapshots in time. However, the LOFS array can record continuously in any weather conditions, thus providing a wealth of data about the ambient seismic field.

Aki (1957) first linked the azimuthally averaged cross-spectrum of micro-tremors to the dispersion of the fundamental-mode Rayleigh wave. Later, Claerbout (1968) devised acoustic daylight imaging, and established a relationship between the autocorrelation of transmission responses to the reflection response of a 1D medium. This technique, turning ambient seismic recordings into virtual seismic sources, has been generalized to 3D and coined seismic interferometry; yielding estimated Green's

Accepted for publication in Geophysical Research Letters

functions (EGFs) by cross-correlation of ambient seismic recordings (Wapenaar and Fokkema, 2004). Convincing applications of this phenomenon have been made in solar physics (Duvall et al., 1993), laboratory acoustics (Weaver and Lobkis, 2001, 2002) and seismology (Campillo and Paul, 2003; Shapiro and Campillo, 2004). Seismologists have used ambient-seismic-noise tomography (ASNT) extensively in regional and global seismic studies to extract surface waves and image the subsurface (Shapiro et al., 2005; Gerstoft et al., 2006; Yao et al., 2006; Lin et al., 2008). These studies use stations that are spaced up to several hundred kilometers apart, and several weeks to months of data are needed to retrieve high quality EGFs by cross-correlation (Seats et al., 2012).

Efforts to image the subsurface on an exploration scale using surface waves have been encouraging (Stewart, 2006; Dellinger and Yu, 2009; Bussat and Kugler, 2011; de Ridder and Dellinger, 2011). Last-mentioned study was supported by a more extensive analysis by Mordret et al. (2013a,b). To date, the application of passive seismic interferometry for 4D seismic monitoring has been thwarted by sparse receiver coverage, insufficient recording time, and routine application of a low-cut filter.

Scholte-wave group velocities derived from controlled-source seismic at Valhall have been shown to be sensitive to production-induced changes (Wills et al., 2008). This can be discerned only through a high degree of experiment repeatability. We investigate which subsurface features can be imaged using seismic noise, and report that relatively short recordings are sufficient to create a high repeatability of Scholte-wave velocity maps using tomography. This repeatability should allow for the design and installation of a system that exploits the ambient seismic noise field to perform continuous and nearly real-time reservoir surveillance.

SCHOLTE-WAVE PASSIVE SEISMIC INTERFEROMETRY AT VALHALL FIELD

Passive seismic interferometry is a technique that cross-correlates ambient seismic recordings from two receiver stations to form a signal as if one of the stations were acting as a seismic source. This correlation signal is termed an estimated Green's function (EGF). We apply this technique to the ambient Scholte-wave energy in the vertical component of particle velocity, recorded just under the seabed by the LOFS array at Valhall. Scholte waves are interface waves that propagate along a solid-fluid interface; their particle motions are in the plane containing the the direction of propagation and the normal to the interface of propagation (i.e. the vertical component) (Scholte, 1942a,b).

Seismic Interferometry

The first assumption for Green's function retrieval by cross-correlation is that the energy flux in the ambient wave field is equipartitioned; i.e., energy flux is inde-

pendent of direction, and all wave modes are excited equally (Lobkis and Weaver, 2001). Modal-energy equipartition alone is not sufficient (Snieder et al., 2010). We require that sources surrounding the station pair act uncorrelated so that the cross-correlation of a long recording time evaluates an ensemble average of the independent contributions of the sources surrounding the station pair (Wapenaar and Fokkema, 2004, 2006).

Let $G^{v,f}_{z,z}(\mathbf{x}_A, \mathbf{x}_B, \omega)$ denote the the frequency-domain elastodynamic Green's function of the vertical component of particle velocity, v, at $\mathbf{x}_A$ due to a vertical external volume force density, f, at $\mathbf{x}_B$. Estimates of the Green's function $G^{v,f}_{z,z}(\mathbf{x}_A, \mathbf{x}_B, \omega)$ and its reciprocal counterpart, $G^{v,f}_{z,z}(\mathbf{x}_A, \mathbf{x}_B, \omega)$, can be retrieved as follows (Wapenaar and Fokkema, 2004):

$$\left\{G^{v,f}_{z,z}(\mathbf{x}_A, \mathbf{x}_B, \omega) + G^{v,f*}_{z,z}(\mathbf{x}_B, \mathbf{x}_A, \omega)\right\} S(\omega) \propto \langle v_z(\mathbf{x}_A, \omega) v^*_z(\mathbf{x}_B, \omega)\rangle \,, \tag{1}$$

where the cross-correlated signals $v_z(\mathbf{x}_A, \omega)$ and $v_z(\mathbf{x}_B, \omega)$ denote vertical components of the particle velocity made at $\mathbf{x}_A$ and $\mathbf{x}_B$ (the master station), respectively. Complex conjugation is denoted by *, and $\langle\rangle$ denotes a spatial ensemble average. The power spectrum of the noise source signals is denoted by $S(\omega)$. Typically, the cross-correlation is not symmetric, reflecting directivity of the ambient seismic field.

In theory, this technique recovers the full elastodynamic Green's function including interface waves, P and S body waves, and single- or multiply-scattered converted waves. In practice, the application of passive seismic interferometry is limited to an ambient-seismic-noise regime that satisfies the aforementioned conditions. These requirements are more often met for surface waves then for other wave modes (Forghani and Snieder, 2010), therefore this study focuses on surface waves.

Cross-Correlation of Valhall LOFS Array Ambient Seismic Scholte-Wave Noise

A recording spanning a little over five days was made from the LOFS in December 2010. Figure 1 shows how the spectrum in the vertical component of particle velocity varies over time. The spectrum was calculated in 2.5-minute overlapping windows and averaged over 153 stations on the northwestern end of the array (where the spectrum is found to have little platform-generated noise). The LOFS array was designed for controlled-source seismic surveying with 15 Hz geophones. But the sensors records ample energy below 2 Hz when the acquisition-standard low-cut filter is turned off.

The spectrum above 2 Hz is dominated by seismic shooting of an acquisition at nearby Ekofisk Field and energy from other human operations, such as boats, drilling and production noise from the Valhall platforms. This platform noise and other human-generated noise dominates the spectrum down to about 2 Hz. This noise radiates mostly from the platform in the center of the array, and therefore is suitable for seismic interferometry only between station pairs oriented aligned with the platform (Landes et al., 2009). The energy at frequencies lower then 2 Hz is known

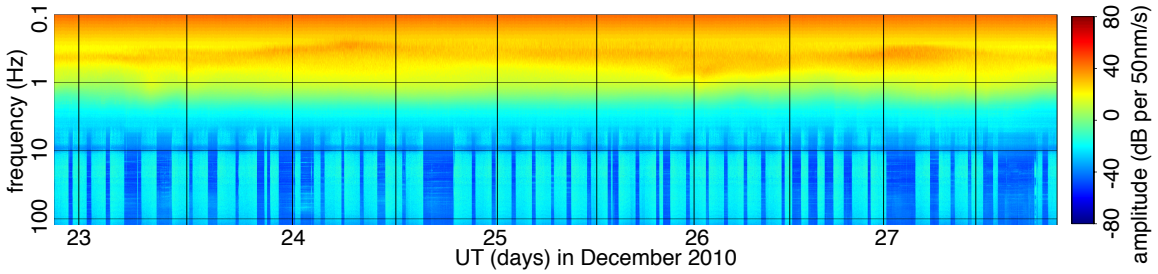

Figure 1: Time-varying spectrum of the five-day passive recording made in 2010. Above 10 Hz, the energy of a seismic acquisition survey at nearby Ekofisk dominates the spectrum. Below 2 Hz, the double-frequency microseism energy band dominates the spectrum. [**CR**]

as microseism energy from the double-frequency microseism peak. This energy is generated by sea swells compressing the seabed (Longuet-Higgins, 1950) and therefore varies with sea depth, wave strength and weather.

The LOFS recordings were bandpassed in 30-minute overlapping windows, with 15-minute increments, under a sine-squared taper. The bandpass was performed in the frequency domain by multiplication with a raised cosine taper, which has coefficients that equal 0 at 0.175 Hz and 1.75 Hz and equal 1 between 0.20 Hz and 1.50 Hz. We form 240 30-minute windows from the five-day long recording. We create a virtual seismic survey by selecting each station as a master station and collecting all virtual seismic sources. We average five sets of 48 virtual seismic surveys from consecutive 30-minute windows to create five independent daily seismic surveys. We average 240 virtual seismic surveys in a five-day virtual seismic survey.

Figure 2a contains a time slice (cross-correlation time-lag $\tau = 6$ s) of a virtual seismic source in the center of the array. The virtual source radiates approximately equally in all directions, indicating that the energy flux in the ambient seismic field at Valhall, after averaging over these five days, was about equally strong in all directions.

The dispersive nature of the Scholte-waves emitted by this virtual seismic source is shown in Figure 2b. This figure is obtained as the amplitude of a Radon (frequency slowness, $\omega - p$) transform of an offset gather of correlations between all station pairs, normalized by frequency. Both the fundamental mode and the first overtone are distinguishable. The seismic interferometry result is dominated by fundamental-mode Scholte waves. This is consistent with Kimman and Trampert (2010), who show that fundamental modes converge faster than higher-order modes. A first overtone that is travelling faster then the fundamental mode, is visible above 0.8 Hz. Recovery of this higher mode is of interest, because higher modes are more sensitive to deeper structure (Aki and Richards, 2002). At lower frequencies (below 0.5 Hz), the fundamental mode jumps to significantly higher velocities, indicative of a sharp velocity increase in the subsurface. The peak between 1.0 ms/m and 2.0 ms/m and between $0.2 - 0.3$ Hz is interpreted as a side lobe (ringing) of the fundamental mode that is created by the

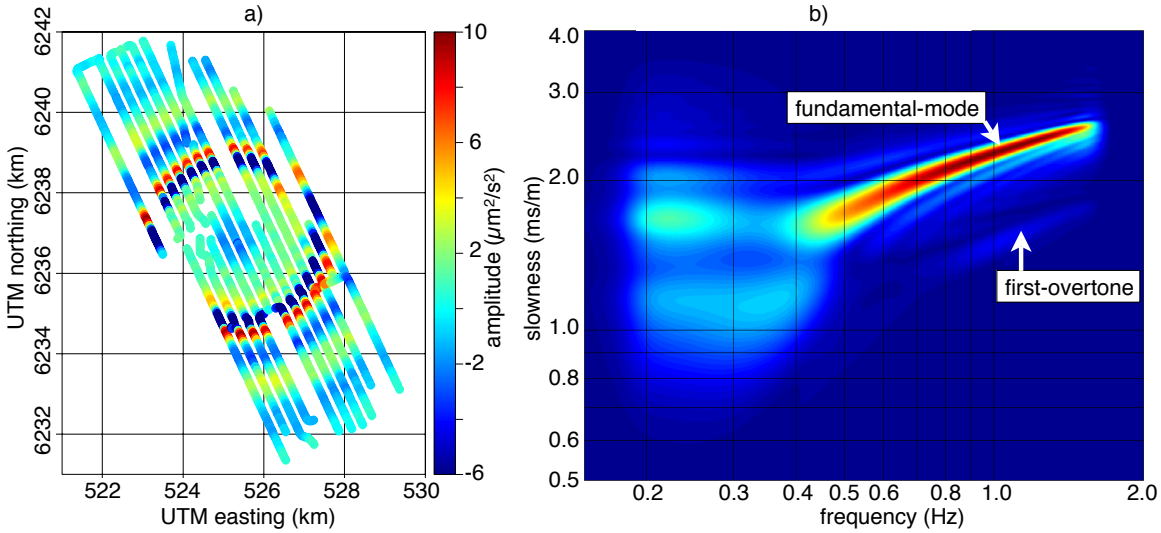

Figure 2: a) Time slice, corresponding to $\tau = 6$ s, of a virtual seismic source located in the center of the array. b) Dispersion image obtained as the amplitude of a Radon $(\omega - p)$ transform, normalized by frequency, of an offset gather of correlations between all station pairs. [**CR**]

$\omega - p$ transformation.

AMBIENT-SEISMIC-NOISE TOMOGRAPHY

We aim to create Scholte-wave group-velocity maps at different frequencies by picking a group traveltime as the peak of the envelope after a narrow-range bandpass. Lower-frequency group-velocities image deeper because lower frequencies have longer wavelengths averaging over deeper structures.

A simple Hann-window bandpass selects a narrow frequency range. After spectral balancing, traveltimes are picked as the maximum of the envelope within a two-second-wide linear move-out window. A quality factor on each pick is defined by a signal-to-noise ratio (SNR) based on the maximum of the envelope within the window divided by the average of the envelope outside the window. Source-receiver pairs with a causal versus anti-causal traveltime difference corresponding to 0.1 ms/m for $0.55 - 1.15$ Hz, and 0.2 ms/m for $1.15 - 1.75$ Hz, are discarded. The accepted travel-time picks are based on a symmetrized EGF. Only source-receiver pairs with a SNR > 3 for $0.55 - 1.15$ Hz or SNR > 1.5 for $1.15 - 1.75$ Hz, and offsets between 2000 m and 6000 m were selected for inversion (about one million traveltime picks for $0.55 - 1.15$ Hz and about six hundred thousand for $1.15 - 1.75$ Hz). For each inversion, we find N travel-time picks, $\mathbf{t} = (t_1, t_2, ..., t_N)^t$, that are predicted from a slowness model space, $\mathbf{m}$, by a straight-ray tomography operator, $\mathbf{F}$. This operator is simply a slowness integration kernel, where each row contains the distances through

each model cell of a line directly from source to receiver, to predict the traveltime of one specific source-receiver couple. The problem is posed as a perturbation, $\Delta\mathbf{m}$, of an average slowness, m_0:

$$\mathbf{m} = \mathrm{m}_0 + \Delta\mathbf{m} \tag{2}$$

$$\mathrm{m}_0 = \frac{1}{N}\sum_{i=1}^{N}\frac{t_i}{\Delta x_i} \tag{3}$$

$$\Delta\mathbf{t} = \mathbf{t} - \mathrm{m}_0\,\Delta\mathbf{x}, \tag{4}$$

where $\Delta\mathbf{x} = (\Delta x_1, \Delta x_2, ..., \Delta x_N)^t$ contains the source-receiver distances for each traveltime, and $\Delta\mathbf{t}$ are the travel-time residuals after the contribution of the average slowness is taken into account. A conjugate-direction algorithm is used to find the minimum of the following L^2 norm:

$$\left\|\mathbf{F}\Delta\mathbf{m} - \Delta\mathbf{t}\right\|_2^2 + \epsilon\left\|\nabla^2\Delta\mathbf{m}\right\|_2^2, \tag{5}$$

where we use the ∇^2 operator as regularization to force a smooth model. The model space is formed by 90 (easterly) by 110 grid cells (northerly) each 100 meters wide. The solver is run till the norm of the data-space and model-space residuals each change less then 0.01% of their respective maximum values. After the first iteration, the 2.5% worst-fit data points are eliminated. The problem is redefined and ran till convergence again for a range of ϵ. The grid cell size is below the resolution of the wavelength thus the regularization plays an important role in finding reasonable solutions. The optimum ϵ is picked, using an L-curve analysis, choosing a value above which the regularization has significantly less influence (Aster et al., 2005).

Group velocity maps for two frequency ranges are shown in Figures 3a and 3b, for $0.55 - 1.15$ Hz and for $1.15 - 1.75$ Hz, respectively. The figures compare five velocity maps from independent, day-long recordings with a velocity map from the complete five-day recording. Both the average RMS difference between the 10 combinations of velocity maps obtained from day-long recordings in Figures 3a and the average RMS difference between the 5 combinations of velocity maps obtained from day-long recordings and the velocity map obtained from the complete five-day recording is ~ 1.1 m/s. The same analysis for 3b results in average RMS differences of ~ 2.0 m/s. This is an indication that the correlation convergence rate at higher frequencies is lower than at lower frequencies, consistent with preliminary results shown by de Ridder (2012).

COMPARISON WITH *P*-WAVE VELOCITY MAPS FROM FULL WAVEFORM INVERSION

The P-wave velocity structure at Valhall is independently well known from regular controlled-source seismic surveying (Sirgue et al., 2010). Two xy-slices through a cube of *P*-wave velocities are shown in Figure 4, panels a and b, for ranges $150 - 195$ m and $105 - 150$ m below the sea floor, respectively. Because these controlled sources cover

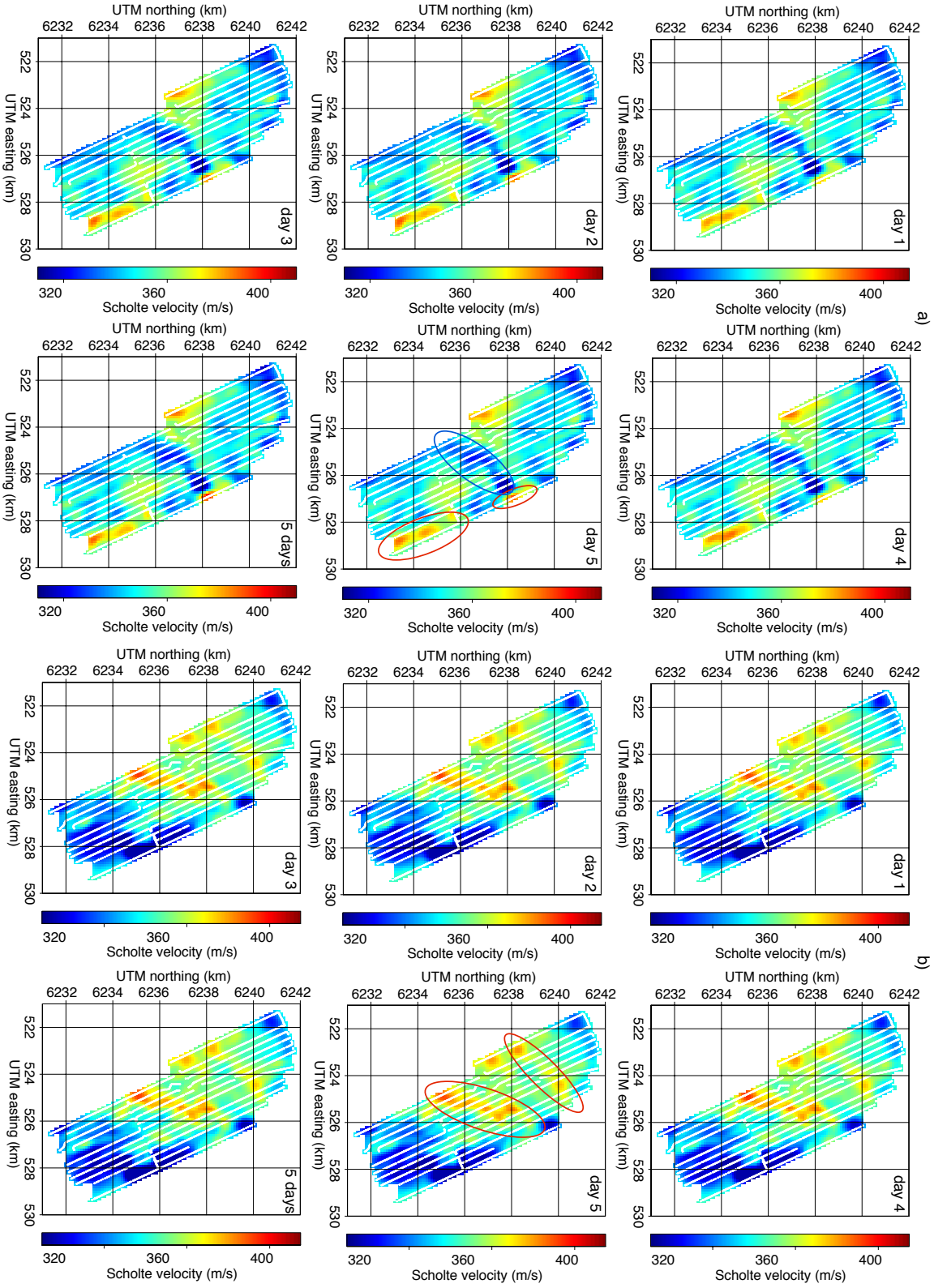

Figure 3: Scholte-wave group-velocity tomography for $0.55-1.15$ Hz in a) and $1.15-1.75$ Hz in b). Both sets contain maps obtained using five independent, day-long passive recordings and a map obtained using the five-day passive recording. In the images for day 5 the high-velocity channels are annotated by red circles, and the sub-platform and channel fill low-velocity zone is annotated by a blue circle. [**CR**]

a wider area than the receiver array, these images include features extending well beyond the area of the receiver array. The maps obtained from ambient-seismic-noise tomography are necessarily confined within the area of the recording array. Based on Figure 2, the wavelengths of the Scholte-waves underlying the the group velocity maps in 3a and 3b are between $190-500$ m and $110-190$ m respectively. Although the Scholte-wave group velocity maps have an integrated sensitivity over depth, they exhibit peak depth-sensitivities of half the wavelength: $85-250$ m and $55-85$ m respectively (Aki and Richards, 2002). Figures 3a and 3b can be compared to the depth slices in Figures 4a and 4b respectively. No unique mapping exists between Scholte-wave velocities and P-wave velocities, but each reflects the underlying geology that shapes the velocity anomalies.

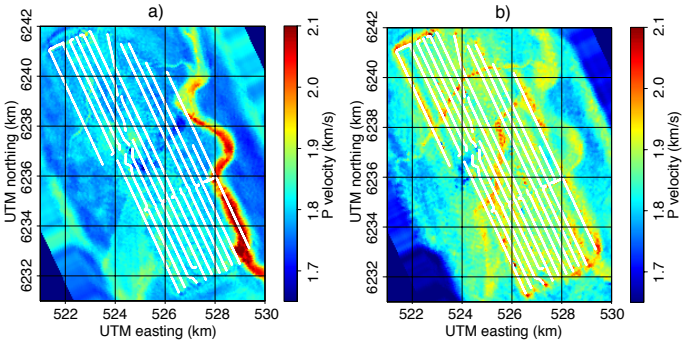

Figure 4: Image of P-wave velocities obtained using waveform inversion of controlled-source P-wave data (Sirgue et al., 2010). Velocity slices $150-195$ m below the sea floor in a) and $105-150$ m below the sea floor in b). [**NR**]

We identify the following similarities between Figures 3a and 4a: a wide channel that crosses within the array boundary at the southeastern corner of the array and again touches the edge of the array near UTM $(526.5, 6239)$ km; a low-velocity zone reflects a combination of channel fill and sub-platform low-velocities stretches across the array from UTM $(525, 6235.5)$ km to UTM $(526.5, 6238)$ km. We identify the following similarities between Figures 3b and Figure 4b: a thinner meandering channel that strikes approximately north-south, approximately from UTM $(525, 6235)$ km to UTM $(526, 6238.5)$ km, and a less well defined channel that crosses the northern end of the array from UTM $(523, 6238.5)$ km to UTM $(525, 6240)$ km. The Scholte-wave velocities in Figure 3b are generally higher in the vicinity of the platform, UTM $(523, 6238.5)$ km, which lies above the central region of the field, than in the southeastern portions of the array. Although not observed in the P-wave velocities of Figure 4, this was identified by Hatchell et al. (2009) in Scholte-wave velocity images from controlled-source seismic and is representative of contractional and extensional strains caused by production-related sea-floor subsidence at Valhall.

The images in Figure 3 are generally smoother than the P-wave velocity images in Figure 4. This is attributed to a combination of the regularization of the velocity map, the wavelength of the interface waves, and the limited depth resolution provided by the dispersive character of the interface waves. These limitations are either less strict or do not apply in the P-wave (body wave) inversions.

CONCLUSIONS

We have shown remarkable repeatability of Scholte-wave group-velocity maps of the overburden at the Valhall Field. We correlate for mere 24 hours to retrieve high-quality EGFs suitable for ambient-seismic-noise tomography. Images of Scholte-wave group velocities obtained using ASNT correspond well with maps of P-wave velocities obtained from controlled-source seismic acquisition and full-waveform inversion. Features as deep as 200 m below the sea floor can be identified from group velocity maps in a frequency range of $0.55 - 1.15$ Hz. Further studies of recordings separated by months are necessary to distinguish long-term changes from daily fluctuations. Careful benchmarking of quality control in the ASNT process could potentially stabilize the daily images such that short-term changes can be reliably identified. Imaging and inversion of EGFs is not limited to ASNT, and more sophisticated inversion methodologies can be developed for virtual seismic sources obtained using dense local receiver arrays. A wide range of practices, including CO_2 sequestration projects, might benefit from successful monitoring by seismic interferometry.

ACKNOWLEDGMENTS

Olav Barkved, Greg Beroza, Jason Chang, Bob Clapp and Joe Dellinger and Dave Nichols for helpful discussions and suggestions. Reviewers Nikolai Shapiro and Matt Haney for comments and suggestions that benefited both this paper and my continued research. BP and the partners of the Valhall Field (BP Norge and Hess Norge) for permission to publish this paper. The sponsors of the Stanford Exploration Project for financial support.

REFERENCES

Aki, K., 1957, Space and time spectra of stationary stochastic waves, with special reference to microtremors: Bulletin of the Earthquake Research Institute, **35**, 415–456.

Aki, K. and P. G. Richards, 2002, Quantitative Seismology - second edition: University Science Books.

Aster, R., B. Borchers, and C. Thurber, 2005, Parameter Estimation and Inverse Problems: Academic Press.

Bussat, S. and S. Kugler, 2011, Offshore ambient-noise surface-wave tomography above 0.1 hz and its applications: The Leading Edge, **30**, 514–524.

Campillo, M. and A. Paul, 2003, Long-range correlations in the diffuse seismic coda: Science, **299**, 547–549.

Claerbout, J. F., 1968, Synthesis of a layered medium from its acoustic transmission response: Geophysics, **33**, 264–269.

de Ridder, S., 2012, Ambient seismic noise correlations for reservoir monitoring: SEG Technical Program Expanded Abstracts, **31**, 1–5.

de Ridder, S. and J. Dellinger, 2011, Ambient seismic noise eikonal tomography for near-surface imaging at valhall: The Leading Edge, **30**, 506–512.

Dellinger, J. A. and J. Yu, 2009, Low-frequency virtual point-source interferometry using conventional sensors: 71st Meeting, European Associated of Geoscientists and Engineers, Expanded Abstracts, X047.

Duvall, T., S. Jefferies, J. Harvey, and M. Pomerantz, 1993, Time-distance helioseismology: Nature, **362**, 430–432.

Forghani, F. and R. Snieder, 2010, Underestimation of body waves and feasibility of surface-wave reconstruction by seismic interferometry: The Leading Edge, **29**, 790–794.

Gerstoft, P., K. P. Sabra, P. Roux, W. A. Kuperman, and M. C. Fehler, 2006, Greens functions extraction and surface-wave tomography from microseisms in southern california: Geophysics, **71**, SI23SI31.

Hatchell, P. J., P. B. Wills, and C. Didraga, 2009, production induced effects on near-surface wave velocities at valhall: 71st Meeting, European Associated of Geoscientists and Engineers, Expanded Abstracts, T016.

Kimman, W. P. and J. Trampert, 2010, Approximations in seismic interferometry and their effects on surface waves: Geophysical Journal International, **182**, 461–476.

Kommedal, J. H., O. I. Barkved, and D. J. Howe, 2004, Initial experience operating a permanent 4C seabed array for reservoir monitoring at Valhall: SEG Technical Program Expanded Abstracts, **23**, 2239–2242.

Landes, M., N. M. Shapiro, S. Singh, and R. Johnston, 2009, Studying shallow seafloor structure based on correlations of continuous seismic records: SEG Technical Program Expanded Abstracts, **28**, 1693–1697.

Lin, F.-C., M. P. Moschetti, and M. H. Ritzwoller, 2008, Surface wave tomography of the western united states from ambient seismic noise: Rayleigh and love wave phase velocity maps: Geophysical Journal International, **173**, 281–298.

Lobkis, O. I. and R. L. Weaver, 2001, On the emergence of the greens function in the correlations of a diffuse field: J. Acoust. Soc. Am., **110**, 3011–3017.

Longuet-Higgins, M. S., 1950, A theory of the origin of microseisms: Phil. Trans. R. Soc. Lond. A, **243**, 135.

Mordret, A., M. Landès, N. M. Shapiro, S. C. Singh, P. Roux, and O. I. Barkved, 2013a, Near-surface study at the Valhall oil field from ambient noise surface wave tomography: Geophysical Journal International.

Mordret, A., N. M. Shapiro, S. Singh, . Roux, J. P. Montagner, and O. I. Barkved, 2013b, Azimuthal anisotropy at Valhall: the Helmholtz equation approach: Geophys. Res. Let.

Scholte, J. G., 1942a, On the stoneley wave equation: Proceedings of the KNAW, **45**, 20–25.

———, 1942b, On the stoneley wave equation: Proceedings of the KNAW, **45**, 159164.

Seats, K. J., J. F. Lawrence, and G. A. Prieto, 2012, Improved ambient noise correlation functions using welch's method: Geophysical Journal International, **188**, 513–523.

Shapiro, N. M. and M. Campillo, 2004, Emergence of broadband rayleigh waves from correlations of the ambient seismic noise: Geophys. Res. Let., **31**, L07614–1–

L07614–4.

Shapiro, N. M., M. Campillo, L. Stehly, and M. R. Ritzwoller, 2005, High-resolution surface-wave tomography from ambient seismic noise: Science, **307**, 1615–1618.

Sirgue, L., O. I. Barkved, J. Dellinger, J. E. U. Albertin, and J. H. Kommedal, 2010, Full waveform inversion: the next leap forward in imaging at Valhall: First Break, **28**, 65–70.

Snieder, R., Y. F. E. Slob, and K. Wapenaar, 2010, Equipartitioning is not sufficient for green's function extraction: Earthquake Science, **23**, 403–415.

Stewart, P., 2006, Interferometric imaging of ocean bottom noise: SEG Technical Program Expanded Abstracts, **25**, 1555–1559.

Wapenaar, K. and J. Fokkema, 2004, Reciprocity theorems for diffusion, flow, and waves.: J. Appl. Mech., **71**, 145–150.

———, 2006, Green's function representations for seismic interferometry: Geophysics, **71**, SI33–SI46.

Weaver, R. L. and O. I. Lobkis, 2001, Ultrasonics without a source: Thermal fluctuation correlations at mhz frequencies.: Phys. Rev. Let., **87**, 134301–1 – 134301–4.

———, 2002, On the emergence of the Green's function in the correlations of a diffuse field: pulse-echo using thermal phonons: Ultrasonics, **40**, 435–439.

Wills, P. B., P. J. Hatchell, and S. J. Bourne, 2008, time-lapse measurements of shallow horizontal wave velocity over a compacting field: 70st Meeting, European Associated of Geoscientists and Engineers, Expanded Abstracts, G039.

Yao, H., R. D. van der Hilst, and M. V. de Hoop, 2006, Surface-wave array tomography in se tibet from ambient seismic noise and two-station analysis i. phase velocity maps: Geophys. J. Int., **166**, 732–744.